Supplementary Information (SI) for Journal of Materials Chemistry A.
This journal is © The Royal Society of Chemistry 2025

Table S1. Specifications of commercial cathode materials and garnet-type cubic LLZTO.

	Molecular Formula	D10 (μm)	D50 (μm)	D90 (μm)	BET (m^2/g)	1^{st} dis-capacity (mAh/g)
LLZTO	$Li_{6.4}La_3Zr_{1.4}Ta_{0.6}O_{12}$		5			
pc-LNMO	$LiNi_{0.5}Mn_{1.5}O_4$	< 1	3-6	<15		>130 (4.95-3.5 V)
pc-LCO	$LiCoO_2$	≥4.0	14.0-18.0	≤45.0	0.10-0.30	≥188 (4.5-3.0 V)
pc-NMC811	$LiNi_{0.8}Co_{0.10}Mn_{0.10}O_2$	5.0±1.0	10.0±2.0	20.0±4.0	0.6±0.3	≥205 (4.3-3.0 V)
pc-NMC532	$LiNi_{0.5}Mn_{0.3}Co_{0.2}O_2$	~ 5	10-14	≤ 25	0.2-0.5	180-185 (4.4-2.7 V)
pc-NMC111	$Li_{1.05}Ni_{0.33}Mn_{0.33}Co_{0.33}O_2$	≥1.7	3.0±0.5	≤7.0	1.35±0.3	≥162 (4.3-3.0 V)
pc-NMC631	$LiNi_{0.67}Mn_{0.28}Co_{0.05}O_2$		13.0±2.0		0.35±0.15	≥170
sc-NMC631	$LiNi_{0.6}Mn_{0.3}Co_{0.1}O_2$	≥1.5	3.3-4.5	5.5-9.5	0.6-1.3	≥185 (4.4-3.0 V)

Note: Based on the molecular formula, polycrystalline $LiNi_{0.67}Mn_{0.28}Co_{0.05}O_2$ is comparable to single-crystalline $LiNi_{0.6}Mn_{0.3}Co_{0.1}O_2$ (sc-NMC631); therefore we label it as pc-NMC631.

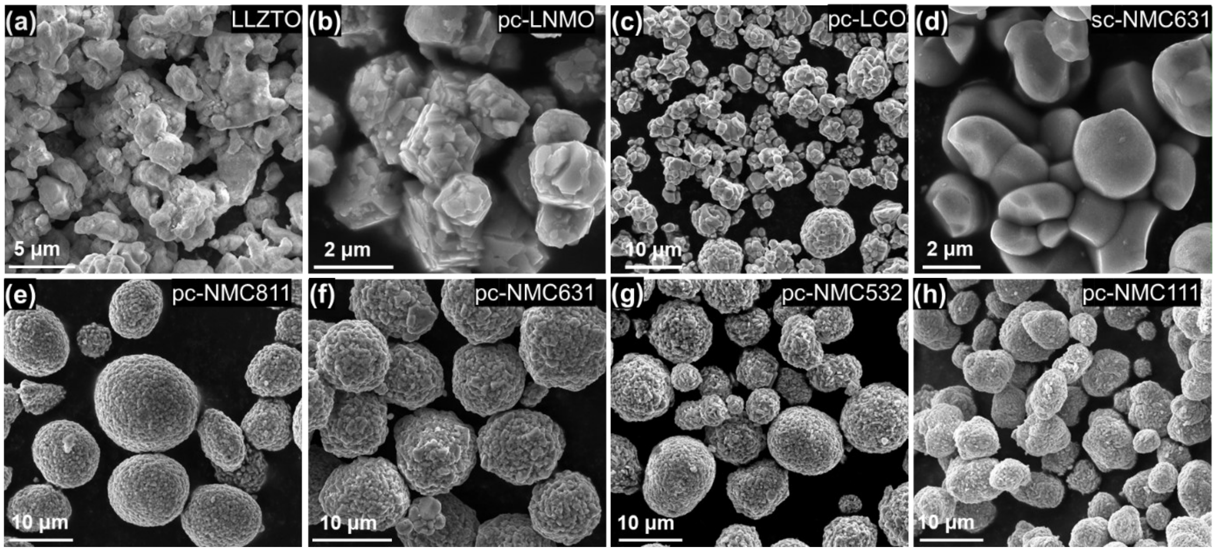

Fig. S1 SEM images of (a) cubic LLZTO and various commercial cathode materials: (b) pc-LNMO, (c) pc-LCO, (d) sc-NMC631, (e) pc-NMC811, (f) pc-NMC631, (g) pc-NMC532, and (h) pc-NMC111.

All materials, including cubic LLZTO and the listed cathode materials, were obtained from commercial suppliers and used as received, without additional treatment. The molecular formula for polycrystalline $LiNi_{0.67}Mn_{0.28}Co_{0.05}O_2$ (pc-NMC631), as provided by the supplier, closely match that of single crystalline $LiNi_{0.6}Mn_{0.3}Co_{0.1}O_2$ (sc-NMC631). Therefore, we examined the impact of crystallographic structure on their electrochemical performance.

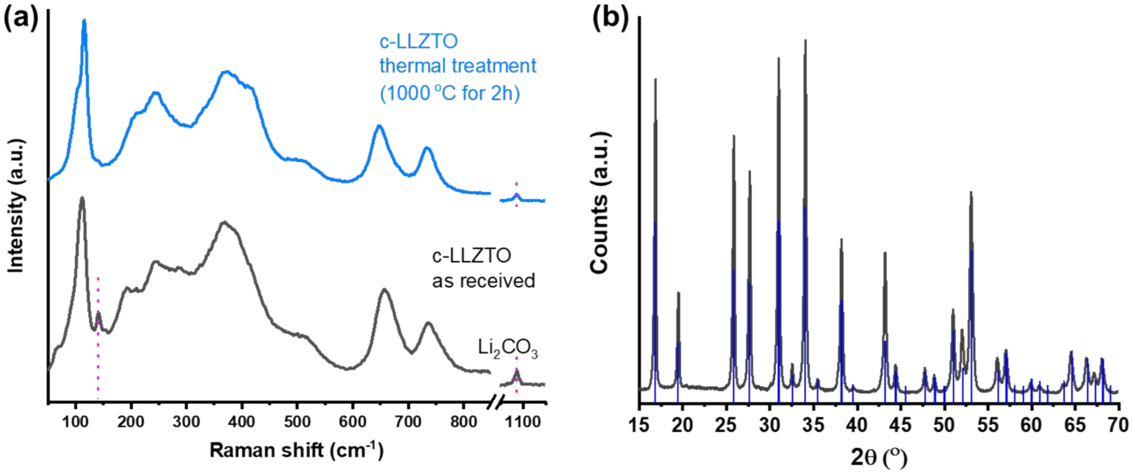

Fig. S2 (a) Raman spectra and (b) XRD pattern of commercial cubic LLZTO.

We compared LLZTO sample before and after thermal treatment at 1000 °C for 2 hours in O_2 amorphous. The Raman spectrum of the as-received sample exhibited more pronounced Li_2CO_3 contamination on the surface.

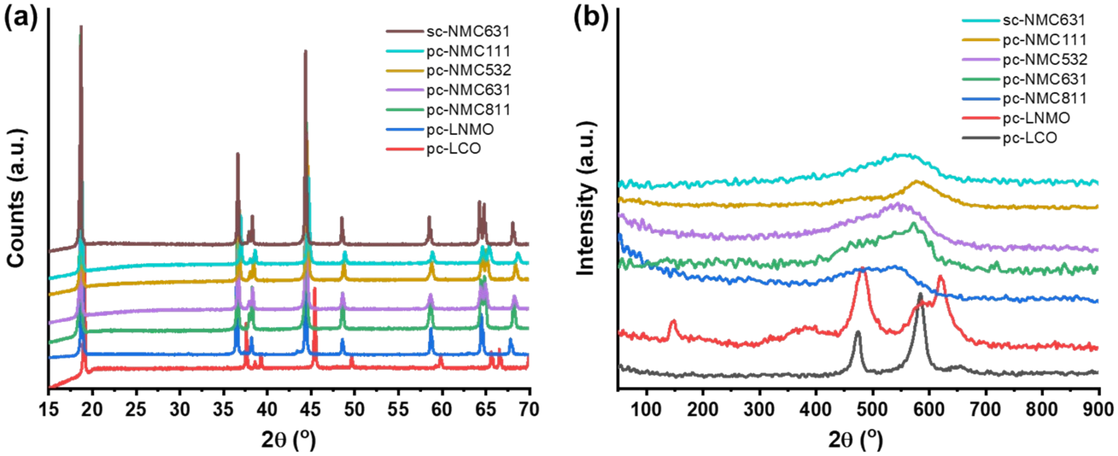

Fig. S3 (a) XRD patterns and (b) Raman spectra of commercial cathode materials.

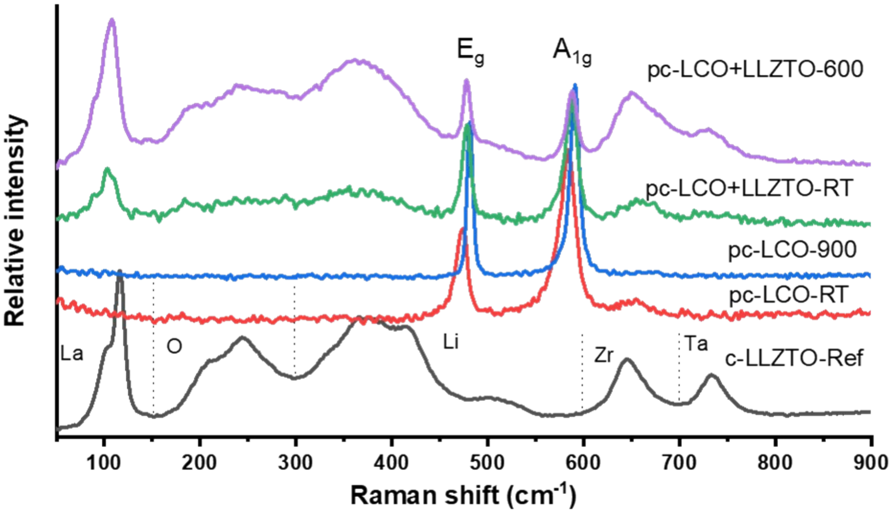

Fig. S4 Raman spectra of pc-LCO heat-treated at 900°C and pc-LCO+LLZTO-600. Reference spectra of pc-LCO-RT, c-LLZTO, and pc-LCO+LLZTO-RT are included for comparison.

The unheated pc-LCO displayed characteristic peaks at 487 cm^{-1} (E_g mode, O-Co-O bending) and 596 cm^{-1} (A_{1g} mode, Co-O stretching). After heat-treatment at 900 °C, both peaks shifted by ~5 cm^{-1} to higher frequencies, indicating modifications in stoichiometry and enhanced crystallinity of pc-LCO.

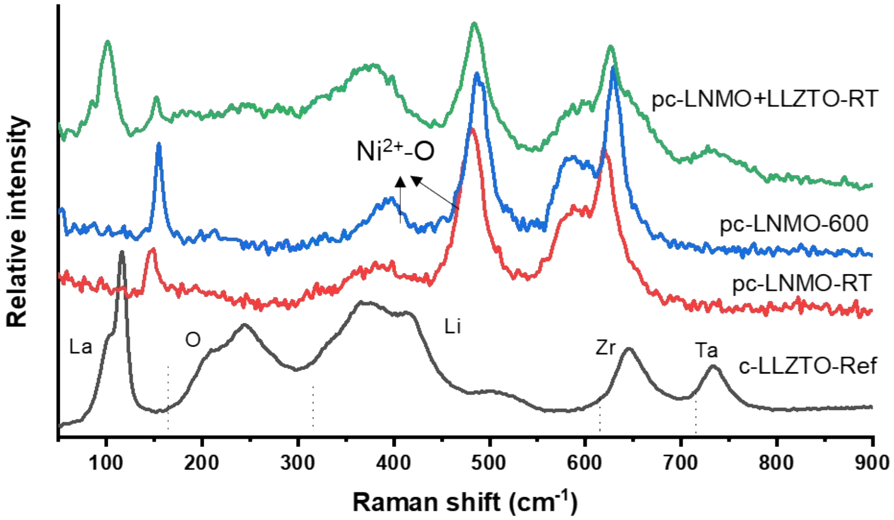

Fig. S5 Raman spectra of pc-LNMO heat-treated at 600°C. Reference spectra of pc-LNMO-RT, c-LLZTO, and pc-LNMO+LLZTO-RT are included for comparison.

The unheated pc-LNMO displayed characteristics Raman bands between 100-700 cm^{-1}, consistent with the A[B_2]O_4 spinel structure and cubic Fd3m symmetry. Notably, the peak at 625 cm^{-1} corresponds to the symmetric Mn-O stretching vibration of [MnO_6] octahedra, while the broad shoulder at 589 cm^{-1} is associated with Ni^{2+} substitution for Mn^{4+}. Additionally peaks at 482 and 393 cm^{-1} are attributed to Ni^{2+}-O stretching vibrations. Following heat treatment at 600 °C, all Raman peaks shifted by ~5 cm^{-1} to higher frequencies, similar to the trend observed in heat-treated LCO, indicating non-stoichiometric changes and improved crystallinity.

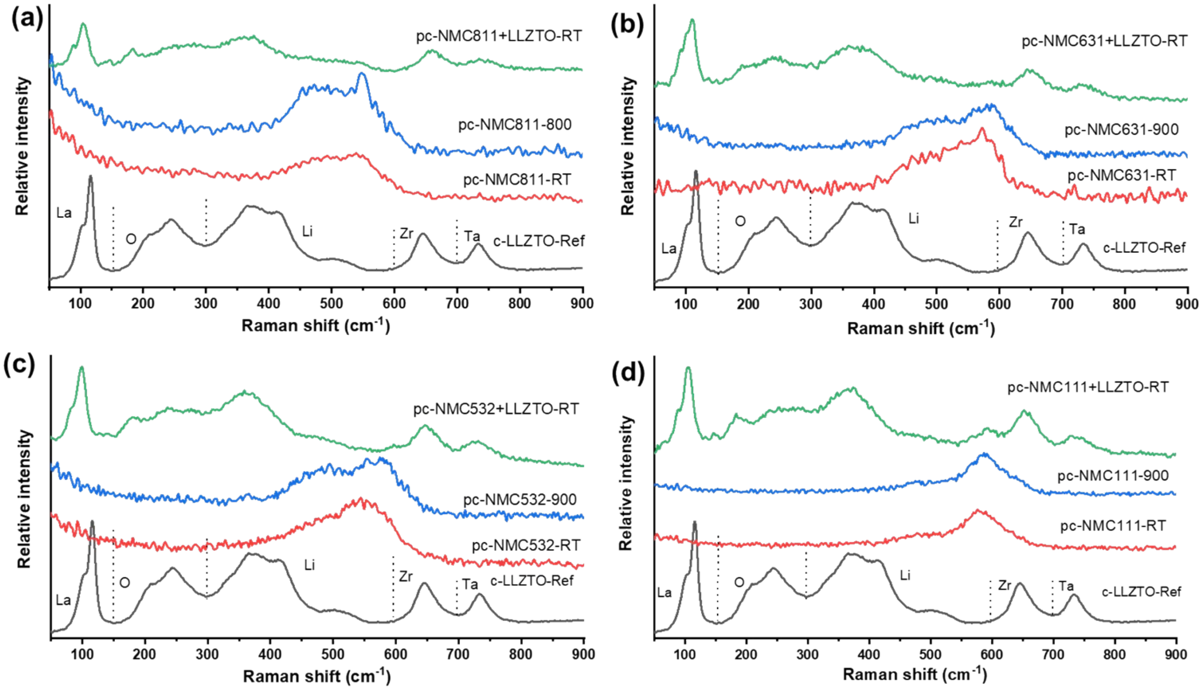

Fig. S6 Raman spectra of (a) pc-NMC811 (b) pc-NMC631, (c) pc-NMC532, and pc-NMC111 before and after heat-treatment. Reference spectra of cubic LLZTO and pc-NMC+LLZTO-RT are provided for comparison.

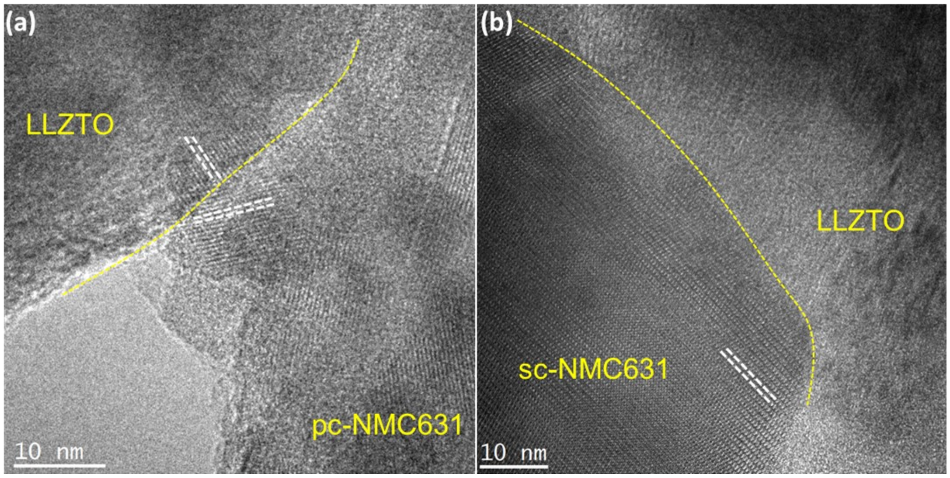

Fig. S7 HR-TEM images of (a) pc-NMC631+LLZTO-900 and (b) sc-NMC631+LLZTO-900.

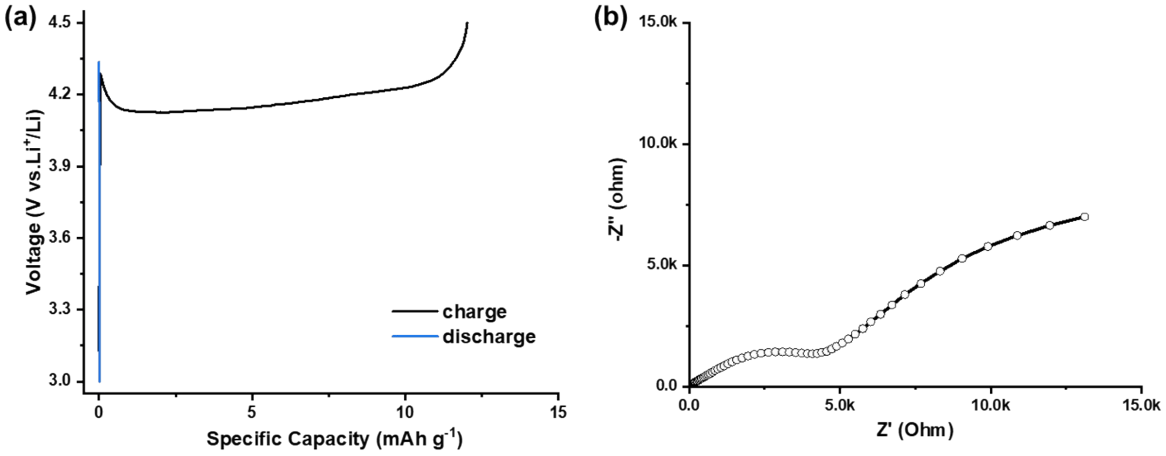

Fig. S8 ASSB based on pc-NMC631+LLZTO-900: (a) charge-discharge profiles at 0.05C and (b) Nyquist plots.

The developed all-solid-state battery exhibits a large charge transfer resistance and significant potential polarization. Unfortunately, it only charged 12 mAh/g capacity then failed.